# Saturation in Conformal Mapping

Martin Hafner, David Franck, and Kay Hameyer
RWTH Aachen University, Institute of Electrical Machines
Schinkelstraße 4, D-52056 Aachen, Germany,
Martin.Hafner@iem.rwth-aachen.de

## 1 Abstract

**Purpose** - In the electromagnetic field simulation of modern servo drives, the computation of higher time and space harmonics is essential to consider appearing torque pulsations, radial forces and ripple torques.
**Design/methodology/approach** - Field computation by conformal mapping techniques is a time-effective method to compute the radial and tangential field components, but it generally neglects the effect of saturation.
**Findings** - This paper presents a method to re-parameterize the conformal mapping approach by single FE computations so as to consider saturation in the model over a wide operation range of the electrical drive.
**Practical implications** - The proposed method is applied to a surface permanent magnet synchronous machine, and compared to numerical results obtained by FEA.
**Originality/value** - An accuracy similar to that of FE simulations can then be obtained with still the low computation time that is the characteristic of analytical models.
**Keywords** - Conformal Mapping, Air-gap permeance, permanent-magnet motors, magnetic fields, design methodology, Air-gap field
**Paper type** - Research paper

## 2 Introduction

The design of electrical machines is routinely done by means of virtual prototyping nowadays, in order to reduce costs and shorten the time-to-market. Besides FEA, which is computationally expensive, analytical models are also used to obtain a quick first approximation of the machine's behavior. Conventional analytical models usually focus on the determination of the fundamental air gap flux density. Consequently, the effect of air gap field harmonics on the main machine characteristics, such as back electromotive force (EMF), cogging-torque and load torque, as well as the impact of geometry variations on those quantities, are neglected. In (Hafner, Franck & Hameyer 2009), the analytic conformal mapping (CM) method in frequency domain for permanent magnet synchronous machines (PMSM) is proposed and applied. The comparison with standard nonlinear FEA shows that it gives a good approximation of the air gap flux distribution, even if minor saturation occurs at local positions. Field harmonics and torque are in good agreement up to nominal current, but start to diverge in current overload situation. In this paper, a method is proposed to cover the effect of saturation on the armature flux density within CM by a FE re-parameterization.

## 3 Standard Conformal Mapping

The air gap field computation by conformal mapping is generally obtained from the solution of a linear Laplace problem, assuming the magnetic core has an infinite permeability. Since this system is linear, the field excitation by magnets and coils, as well the influence of the slotting, can be modeled individually.

Assuming first a slotless stator, the two-dimensional field $\vec{B}\left(\Theta\right)$ at a certain coordinate angle $\Theta$ in the air gap, $\Theta \in [0, 2\pi[$,consists of a radial flux density $B_r\left(\Theta\right)$ and a tangential flux density $B_\varphi\left(\Theta\right)$

$$\vec{B}\left(\Theta\right) = B_r\left(\Theta\right) \cdot \vec{e}_r + B_\varphi\left(\Theta\right) \cdot \vec{e}_\varphi. \tag{1}$$

The angle dependent quantities $B_r\left(\Theta\right)$ and $B_\varphi\left(\Theta\right)$, can be expanded into a Fourier Series

$$\vec{B}\left(\Theta\right) = \sum_{n=0}^{\infty} \left(B_{r,n} \cdot \vec{e}_r + B_{\varphi,n} \cdot \vec{e}_\varphi\right) e^{\jmath np\Theta}, \tag{2}$$

where $n$ is the frequency order and $p$ the number of pole pairs. In this representation of the air gap field, the Fourier coefficients $B_{r,n}$ and $B_{\varphi,n}$ are the solution of a linear Laplace problem with magnets and a slotless stator depending on the magnetization type (Zhu & Howe 1993), (Zhu, Howe & Chan 2002), (Hanselman 2003). The field at a certain instance of time $t$ due to rotor movement is given by

$$\vec{B}\left(t\right) = \vec{B} \cdot e^{\jmath\omega_r t} \tag{3}$$

where $\omega_r$ is the angular speed of the rotor.

Stator slotting significantly influences the magnetic field distribution. It is standardly modeled by "permeance functions". These 2D permeance functions $\vec{\lambda}$ consider the radial and tangential impact of slotting on the slotless field distribution and can be obtained by Schwarz-Christoffel transformations (Zarko, Ban & Lipo 2006), (Zarko, Ban & Lipo 2008). Correlating the field distribution with slotting, ${}^{s}\vec{B}\left(t\right)$, with the field without slotting (3), yields the vectorial permeance $\vec{\lambda}$

$$\begin{aligned} {}^{s}\vec{B}\left(t\right) &= \vec{\lambda}^{*} \cdot \vec{B}\left(t\right) && (4) \\ \vec{\lambda}^{*} &= \begin{pmatrix} \lambda_r & \lambda_\varphi \\ -\lambda_\varphi & \lambda_r \end{pmatrix}. && (5) \end{aligned}$$

The magnetic field distribution due to a current in a single slot, assuming a infinite slot depth and a infinite permeability in a slotless stator, can be obtained analytically by three successive conformal mappings (Binns 1963), named current ansatz function. According to the stator winding scheme, a flux distribution ${}^{p}\vec{B}$, in function of the effective number of winding turns and the coil current, representing the flux distribution per phase can be found from that. The overall armature field ${}^{a}\vec{B}\left(t\right)$ is given by

$${}^{a}\vec{B}\left(t, I\right) = \begin{pmatrix} {}^{p}\vec{B}\left(\sqrt{2}Ie^{\jmath\omega_s t+0^\circ}\right) \\ {}^{p}\vec{B}\left(\sqrt{2}Ie^{\jmath\omega_s t+120^\circ}\right) \\ {}^{p}\vec{B}\left(\sqrt{2}Ie^{\jmath\omega_s t+240^\circ}\right) \end{pmatrix} \cdot \begin{pmatrix} e^{\jmath\phi_q+0^\circ} \\ e^{\jmath\phi_q+120^\circ} \\ e^{\jmath\phi_q+240^\circ} \end{pmatrix}, \tag{6}$$

Table 1: Parameters for Sizing and Electromagnetic Evaluation

| | | |
|---|---|---|
| $p$ | 3 | Number of Pole Pairs |
| $N_s$ | 18 | Number of Stator Teeth |
| $P_r$ | 1520 W | Rated Power |
| $n_r$ | 3000 rpm | Rated Speed |
| $\tau p$ | 0.73 | Pole Pitch Factor |
| $h_m$ | 3 mm | Permanent Magnet Height |
| $r_{orr}$ | 24.5 mm | Outer Rotor Radius (inc. PM) |
| $h_\delta$ | 0.8 mm | Air Gap Height |
| $h_{stth}$ | 0.5 mm | Stator Tooth Tip Height |
| $h_{sth}$ | 21.7 mm | Stator Tooth Height |
| $r_{osr}$ | 54.2 mm | Outer Stator Radius |
| $h_{stw}$ | 5 mm | Stator Tooth Width |
| $h_{sow}$ | 1.5 mm | Slot Opening Width |
| $l_z$ | 101 mm | Length |
| $B_r$ | 1.244 T | Remanence Flux Density |
| $k_{cu}$ | 30 % | Copper Fill Factor |

where the angle $\phi_q$ defines the relative phase orientation to the quadrature axis of the machine and $\omega_s$ is the stator current angular frequency. Due to the governing equation of the current ansatz function in (Binns 1963), the impact of $\vec{\lambda}$ is already considered in the definition of ${}^{p}\vec{B}$. We shall in the sequel systematically omit the arguments $\Theta$ and $t$ and retain only the argument $I$ for all quantities that are current dependent. We shall also label the quantities obtained by the conformal mapping approach with a $CM$ exponent. The overall air gap field by following the procedure explained above is thus defined as

$$ {}^{g}\vec{B}^{CM}(I) = {}^{a}\vec{B}^{CM}(I) + {}^{s}\vec{B}^{CM}. \tag{7}$$

# 4 Saturation in Conformal Mapping

The PMSM studied here, is identical to the machine in (Hafner et al. 2009), where in addition to the construction details the cross section of the motor and the nonlinear $B-H$ characteristic can be found. All parameters of the geometry and the electromagnetic evaluation are given in Table 1.

Equation (4) and (6) represent the analytic air gap flux density distribution for the load and no-load case. Since CM technique assumes an infinite lamination permeability, a deviation between a field characteristic by CM and nonlinear FEA is expected in case of saturation in parts of the ferromagnetic core. Figure 1 shows the absolute deviation in the flux density distribution between CM and FEA in the air gap over a pole pitch with the current $I$ ranging from zero to four times nominal current $I_n$. The deviation in tangential direction (Fig. 1(b)), as well as the radial flux density deviation (Fig. 1(a)) both increase as the current $I$ increases. Moreover, the comparison of load and no-load cases shows that saturation beneath the tooth tips (110°,130°) is already present for a coil current equal to zero, but strongly increases in function of $I$.

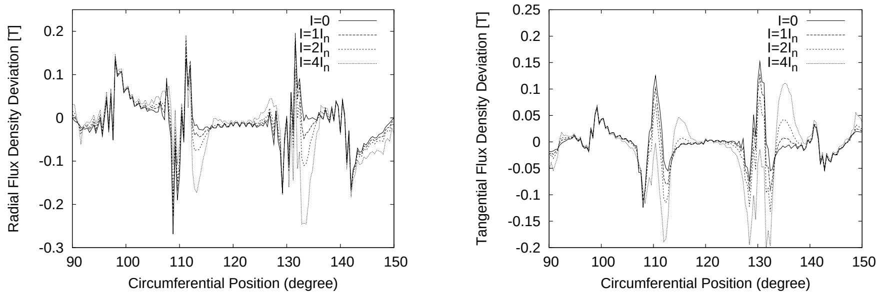

(a) $\Delta B_r = {B_r}^{CM} - {B_r}^{FEA}$

(b) $\Delta B_\varphi = {B_\varphi}^{CM} - {B_\varphi}^{FEA}$

Figure 1: Absolute radial and tangential flux density deviation between CM and FEA over PMSM pole pitch for different load situations.

## 4.1 Methodology

The general idea of this work is to minimize the load dependent deviation shown in Fig. 1 by adding correction terms obtained from FE computations. The current dependent fraction of the saturation is linked with ${}^{a}\vec{B}\,(I)$, whereas the no-load saturation in ${}^{s}\vec{B}$ arises from $\vec{\lambda}$, which does not take into account the reduction of the permeance due to a finite permeability of the lamination, nor the local variation of the permeance due to saturation. Here, the flux deviation due to current dependent saturation should be considered. The computation of correction terms between CM and FEA is carried out in the two-dimensional frequency domain (2D-FFT) over one electrical period in order to consider also the quasi-static flux variation caused by the rotor movement. This 2-dimensional space has the circumferential wave number $\nu$ and the frequencies $f$ for coordinates. The radial and tangential components of the air gap flux density at a certain time step $t$ at the position $\Theta$ is reconstructed from the 2D-FFT space by:

$$B_x(t,\Theta) = \sum_f \sum_\nu \underline{B}_x(\nu, f) e^{-2\pi \jmath (f\cdot t + \nu\cdot\Theta)}\Big|_{x=r,\varphi}, \tag{8}$$

where the coefficients $\underline{B}_x(\nu, f)$ are complex.

This Fourier representation is applied to the CM air gap field ${}^{a}\vec{B}^{CM}\,(I)$ defined above, as well as to the FE calculated armature air gap field defined as:

$${}^{a}\vec{B}^{FEA}\,(I) = \vec{B}^{FEA}\,(I) - \vec{B}^{FEA}\,(I \equiv 0), \tag{9}$$

so that the no-load saturation does not contribute to ${}^{a}\vec{B}^{FEA}\,(I)$ as postulated in the considerations of this methodology. All quantities obtained from FE computations are labeled with a $FEA$ exponent. According to (8), the armature fields ${}^{a}\vec{B}^{CM}\,(I)$ and ${}^{a}\vec{B}^{FEA}\,(I)$ are transformed to the 2D frequency domain to obtain their harmonic representation ${}^{a}\underline{B}_{x}{}^{CM}$, ${}^{a}\underline{B}_{x}{}^{FEA}$. Comparing the frequency domain of CM and FEA for each 1-D wave $(\nu, f)$, two situations can occur:

1. A complex wave $\underline{B}$ changes its amplitude or phase, which can be described by
$$\underline{c}_{x}(\nu, f) = \frac{{}^{a}\underline{B}_{x}{}^{FEA}(\nu, f)}{{}^{a}\underline{B}_{x}{}^{CM}(\nu, f)}, \tag{10}$$
where $\underline{c}_{x}$ is a complex correlation factor. A change in $\Re\left\{\underline{c}_{x}\right\}$ indicates a change of the amplitude, whereas $\Im\left\{\underline{c}_{x}\right\}$ implies a phase shift between both waves.

2. Since saturation modes, classically $\nu = 3p, 5p, 7p$, are not present in CM (Jacob 1998), (10) and can not be applied in this situation (division by zero). Here, the corresponding wave $(\nu, f)$ has to be added in such a way that
$${}^{a}\underline{B}_{x}{}^{CM} + \underline{B}_{x}{}^{Add} = {}^{a}\underline{B}_{x}{}^{FEA}\Big|_{I = I_{Add}}, \tag{11}$$
where the quantity $\underline{B}_{x}{}^{Add}$ is taken from the FEA computation at one certain current load situation $I_{Add}$. Defining the complex factor $\underline{c}_{x}$ in the sense of (10), yields
$$\underline{c}_{x}(\nu, f) = \frac{{}^{a}\underline{B}_{x}{}^{FEA}(\nu, f)}{\underline{B}_{x}{}^{Add}(\nu, f)}. \tag{12}$$

Assuming now that the Fourier coefficients ${}^{a}\underline{B}_{x}{}^{FEA}(\nu, f)$ and ${}^{a}\underline{B}_{x}{}^{CM}(\nu, f)$ are scaling linearly with $I$, the shape of the amplitude of $\underline{c}_{x}$ in function of the current $I$, depends on the calculation rule (10) and (12). In this case, $(\nu, f)$-waves present in ${}^{a}\underline{B}_{x}{}^{CM}(\nu, f)$ are constant, whereas waves existing in $\underline{B}_{x}{}^{Add}(\nu, f)$ scale linearly by $I$, as depicted in Fig. 2. The abscissa of the intersection point between both lines defines $I = I_{Add}$. The field computation by CM including saturation follows in 2D FFT space by modifying (7) with the terms (10) and (12)
$${}^{g}\underline{B}_{x}^{MOD-CM}(I) = {}^{s}\underline{B}_{x}^{CM} + \left({}^{a}\underline{B}_{x}^{CM}(I) + \underline{B}_{x}^{Add}\right) \cdot \underline{c}_{x}(I), \tag{13}$$
where the complex amplification factors of $\underline{c}_{x}$ can be interpolated by a linear or cubic spline. In this work, a linear spline interpolation is applied which requires, besides $I = 0$, at least one sampling point.

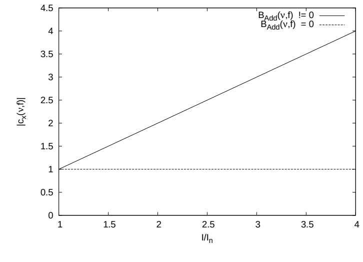

Figure 2: Ideal characteristic of the magnitude of $\underline{c}_{x}$ in function of the normalized phase current I.

## 4.2 Implementation of Methodology

The modeling of saturation within CM bases on adding current dependent phase and amplitude information from a non-linear FE solution. The concept, given in section 4.1, is carried out in the two-dimensional frequency domain to treat each $(\nu, f)$-wave separately. On the one hand, this allows a detailed interpolation of the air gap flux density, but with a loss of simplicity. Moreover, (10) and (12) may face mathematical difficulties, e.g. singularities, which can lead to an instability within the proposed algorithm. Therefore, this section improves the computation of the complex $\underline{c}_x$-factor to avoid instability and minimize the number of non-zero stored correction terms.

The denominator of (10) ${}^a\underline{B}_x{}^{CM}(\nu, f)$, arises from the Fourier spectrum of the sampled values of the continuous and ideal armature field distribution. Since the field revolves by an $e^{\jmath\omega t}$ operator in time, only the fundamental synchronous frequency $f_1$ is present. The magnitude of the $\nu$-waves decrease by an increasing value of $\nu$, leading to infinite values of (10). Introducing a threshold filter function $\mathfrak{F}$, measuring and weighting the relative impact of each wave contribution with respect to the fundamental wave of its operant, defined as

$$\begin{aligned} \mathfrak{F}_{th1} &= \begin{cases} 0, & \text{if } A \leq th1 \\ \underline{B}(\nu, f), & \text{if } A > th1 \end{cases} && (14) \\ A &= \left| \frac{\underline{B}(\nu, f)}{\underline{B}\,(\nu \equiv p, f \equiv 1)} \right|, && (15) \end{aligned}$$

where $th1$ is the threshold, (10) can be rewritten with the reduces spectrum $\mathfrak{F}_{th1}\left\{{}^a\underline{B}_x^{CM}(\nu, f)\right\}$, yielding

$$\underline{c}_x = \frac{{}^a\underline{B}_x^{FEA}(\nu, f)}{\mathfrak{F}_{th1}\left\{{}^a\underline{B}_x^{CM}(\nu, f)\right\}}. \tag{16}$$

The FE electromagnetic governing equations use usually first-order vector potential formulations, leading to zero-order magnetic flux density solutions. This discontinuity in the FE flux density distribution involves that almost all wave components of ${}^a\underline{B}_x^{FEA}$ in (11) are present, giving a dense add-term matrix with many entries of roundabout zero. To avoid a singularity in (12), these add-term entries have to be weighted with respect to their origin in ${}^a\underline{B}_x^{FEA}$. Applying the preprocessor $\mathfrak{F}$ to (12) requires a modification in (11) to

$$\underline{B}_x^{Add} = \mathfrak{F}_{th1}\left\{{}^a\underline{B}_x^{FEA} - {}^a\underline{B}_x^{CM}\right\}\bigg|_{I=I_{Add}}. \tag{17}$$

# 5 Application

The concept presented in section 4 is used to re-parameterize CM by FEA. In minimum, one single FE current-load solution, e.g. for nominal current, is required. To study the behavior of the extracted correction terms representing the saturation of the steel lamination, the presented methodology is carried out for a phase current $I$ in range from one to four times nominal current $I_n$. The crosssection of the motor is pictured in Fig. 1(a) of (Hafner et al. 2009), all parameters of the dimension and the electromagnetic evaluation are in listed in

Table 1. The add-term extraction is carried out for nominal current $I_n$. The threshold $th1$ is set to 1%.

Initially, the occurring additional waves are computed by (17). Figure 3(a) shows the radial amplitude spectrum of the FE-simulation for nominal current in function of the wave coefficient $\nu$ and $f$. Its separation into the fraction ${}^{a}\underline{B}_r^{CM}$ obtained by (17) and the resulting add-term fraction $\underline{B}_r^{Add}$ is depicted in Fig. 3(b).

The evaluation of (17) leads to 23 coefficients in radial and 39 entries in tangential direction. The computation of the correction factors $\underline{c}$ by (12) and (16) gives 10 additional terms for radial and 15 terms for tangential direction. Table 2 lists all $\underline{c}$ terms for the radial component with its space and frequency harmonic and their affectation to ${}^{a}\underline{B}_r^{CM}$ (CM) or $\underline{B}_r^{Add}$ (Add).

According to (Seinsch 1992), the modes of the winding field of the fundamental frequency $f_1$ are given in this example by

$$\nu = p \cdot (1 + 6 \cdot g)\,, \; g = 0, \pm 1, \pm 2, .. \tag{18}$$

and the occurring saturation wave mode follow:

$$\nu = p \cdot \left( \frac{6 \cdot g}{N_q} \begin{matrix} +3 \\ -1 \end{matrix} \right), \text{ for } \begin{matrix} f & = & 3 \cdot f_1 \\ f & = & f_1 \end{matrix} \tag{19}$$

The column "origin" in Table 2 categorizes the wave modes by (18) represented by (w), (19) identified with (Sat) and the unknown groups Gr1, Gr2 and Gr3. All saturation terms for the analytic armature field are, as expected, linked with (18). For the fundamental frequency $f_1$ as well as for the third harmonic $f_3$ 6 wave modes can be identified with (19). Since space harmonics with a rational number of $p$ are implausible in this machine example, group Gr3 has to be considered as numeric noise within the sampled FE field. Group Gr2 with a time frequency of five may be identified as second time-harmonic of the lamination permeance with generally occur as even time frequency multipliers. The modes of Gr1 have a high $\nu$ order and can not be correlated with a standard field harmonic from literature. Figure 4 shows the quantitative change of magnitude and phase of some wave modes of the winding field (w) in function of the load current. As expected when saturation is present, these waves are damped as the load current $I$ increases. The saturation wave modes $(3p, 3f)$ and $(5p, 5f)$ present in the add-term (extracted for nominal current) exhibit a strong linear increase in the magnitude and in case of $(5p, 5f)$ a significant angular phase shift in function of the current, as depicted in Fig. 5.

To demonstrate the effectivity of this method to minimize the current dependent mismatch between FEA and CM, Fig. 6 shows the same deviation as Fig. 1 without the flux density of the permanent magnets. Figure 7 illustrates the field difference in radial and tangential direction after applying the saturation correction to the CM method. It can be observed, that the maximal peak deviation in radial direction beneath the teeth tips (110°and 130°) is reduced from 0.25 T to below 0.08 T, cf. Fig. 6(a) and Fig. 7(a). In tangential direction the minimization of the percentage deviation exhibits to be even stronger from at least 0.2 T to 0.02 T, cmp. Fig. 7(a) and Fig. 7(b).

The analytic field computation by standard conformal mapping, the extraction of the complex corrector factors by already present FEA computation, as well as the modeling of saturation into the armature field, last on a Quad-Core

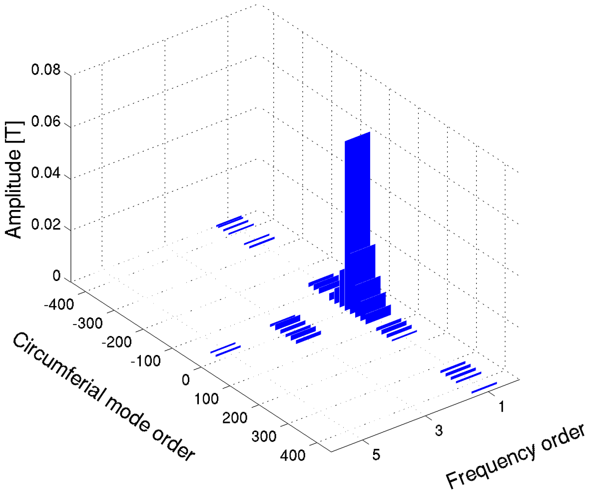

(a) Radial FEA winding field ${}^{a}\underline{B}_r^{FEA}$.

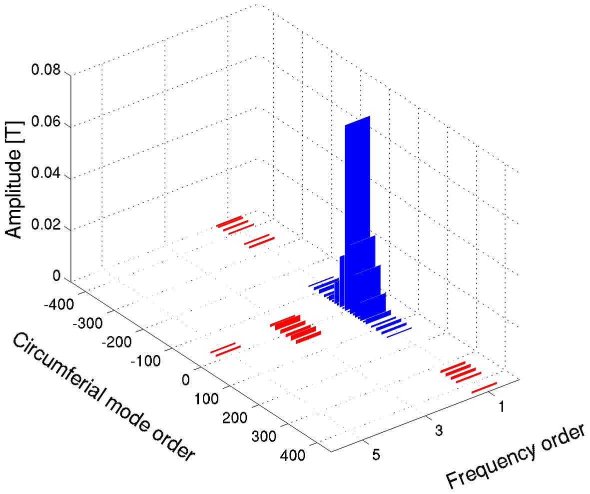

(b) Radial flux density ${}^{a}\underline{B}_r^{FEA}$ separated in the ${}^{a}\underline{B}_r^{CM}$ (Blue) and $\underline{B}_r^{Add}$ (Red)

Figure 3: Amplitude spectrum of add-term fraction $\underline{B}_r^{Add}$ for nominal current computed by (17).

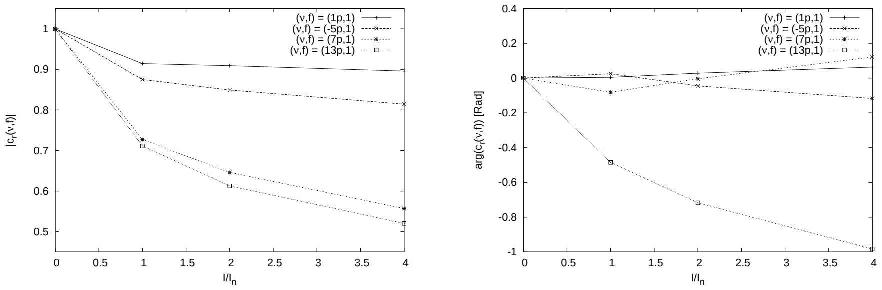

(a) Magnitude of correction factors. (b) Phase of correction factors.

Figure 4: Amplitude and phase of the complex correction factors for armature field (w) in function of load current.

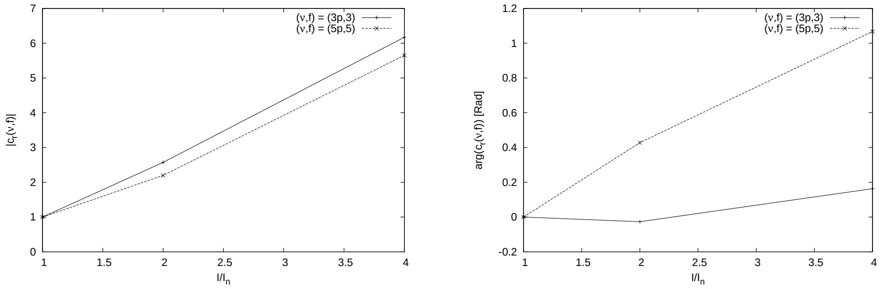

(a) Magnitude of correction factors. (b) Phase of correction factors.

Figure 5: Amplitude and phase of the complex correction factors for armature field (w) in function of load current.

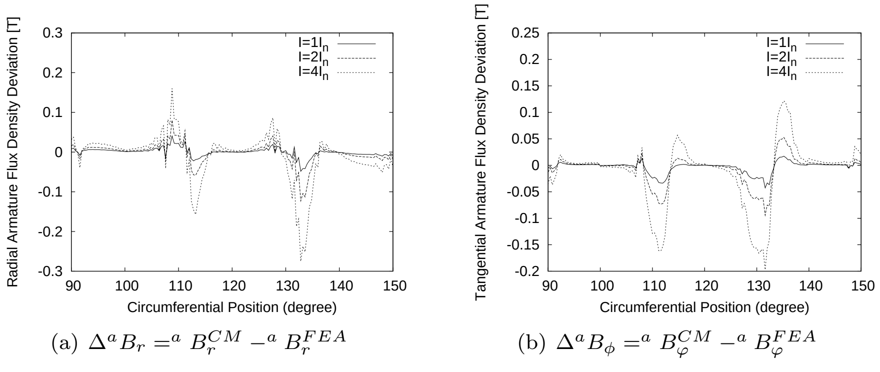

(a) $\Delta^a B_r =^a B_r^{CM} -^a B_r^{FEA}$ (b) $\Delta^a B_\phi =^a B_\varphi^{CM} -^a B_\varphi^{FEA}$

Figure 6: Absolute radial and tangential armature flux density deviation between the CM and FEA over PMSM pole pitch for different load situations.

Table 2: Complex Saturation Factor for Radial Field Correction

| Nr. | $f$ | $\nu$ | Affectation | Origin |
|---|---|---|---|---|
| 1 | 1 | -5p | CM | w |
| 2 | 1 | -11p | CM | w |
| 3 | 1 | -17p | CM | w |
| 4 | 1 | -23p | CM | w |
| 5 | 1 | 43p | CM | w |
| 6 | 1 | 37p | CM | w |
| 7 | 1 | 19p | CM | w |
| 8 | 1 | 13p | CM | w |
| 9 | 1 | 7p | CM | w |
| 10 | 1 | 1p | CM | w |
| 11 | 1 | -119p | Add | Sat |
| 12 | 1 | -115 | Add | Sat |
| 13 | 1 | -121p | Add | Sat |
| 14 | 1 | -127p | Add | Sat |
| 15 | 1 | -145p | Add | Sat |
| 16 | 1 | 149p | Add | Sat |
| 17 | 1 | 147p | Add | Gr1 |
| 18 | 1 | 141p | Add | Gr1 |
| 19 | 1 | 135p | Add | Gr1 |
| 20 | 1 | 117p | Add | Gr1 |
| 21 | 1 | 111p | Add | Gr1 |
| 22 | 3 | -3p | Add | Sat |
| 23 | 3 | -9p | Add | Sat |
| 24 | 3 | -15p | Add | Sat |
| 25 | 3 | 15p | Add | Sat |
| 26 | 3 | 9p | Add | Sat |
| 27 | 3 | 3p | Add | Sat |
| 28 | 5 | 11p | Add | Gr2 |
| 29 | 5 | 5p | Add | Gr2 |
| 30 | 12 | -89,6p | Add | Gr3 |
| 31 | 12 | -95,6p | Add | Gr3 |
| 32 | 14 | -101,6p | Add | Gr3 |
| 33 | 14 | -99,6p | Add | Gr3 |

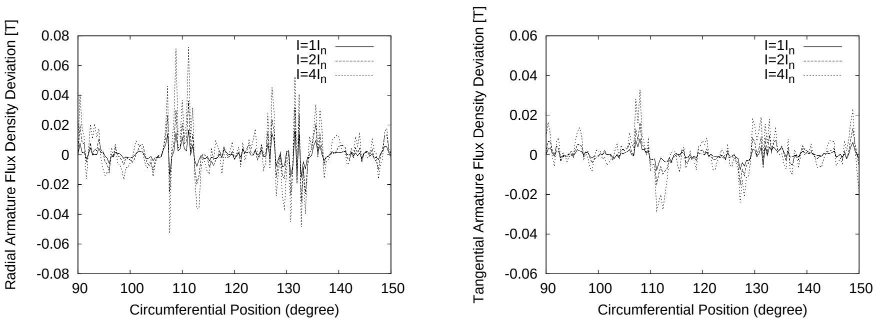

(a) $\Delta^a B_r = {}^a B_r^{Mod} - {}^a B_r^{FEA}$

(b) $\Delta^a B_\phi = {}^a B_\varphi^{Mod} - {}^a B_\varphi^{FEA}$

Figure 7: Absolute radial and tangential armature flux density deviation between the modified CM and FEA over PMSM pole pitch for different load situations.

AMD Opteron Processor with 2,200 MHz in single core usage a few seconds, which is in any case much less than the complete FE computations would require.

# 6 Evaluation and Further Prospects

The method proposed in 4 aims on adopting the phenomena of saturation in the current dependent armature field of CM. The application of the computed correction factors $\underline{c}$ leads to a significant reduction of the mismatch in case of high saturated operation points, cmp. Fig. 6 and Fig. 7. Since the equation of the analytic armature field implicitly models the complex permeance function $\underline{\lambda}$, the correction terms remodulate the time and local dependent variation of $\underline{\lambda}$ over one electrical period in this quantity. In order to set up a correction of the allover air gap flux density field the presented method, can be applied to the explicitly determined permeance $\underline{\lambda}$ in (4) and on the armature field separately. This straight forward approach would indeed lead to sufficient result, but reflects a physically wrong identification of the saturation since both field fraction would be treated differently. Since the described extraction procedure has shown to be target oriented, in a further research the implicit $\underline{\lambda}$ formulation of (6) can be neutralized to end up with one physical modulation of the permeance state description of the machine.

Since the occurring wave modes obtained from FEA have to be evaluated with respect to their physical feasibility, cmp. Table 2, further investigations are necessary to find a better appropriate filter replacing the threshold filter mechanism. In present state the applied saturation model does not consider a change in the phase orientation of the applied current to represent the operation in the field weakening range. To gain insight into the spectral decomposition of radial and tangential forces which can be determined from the CM field combination, the method proposed here can be combined with space vector representations to analyze the participating flux density waves for certain force harmonics, (Rothe, van der Giet & Hameyer 2009), (van der Giet, Rothe & Hameyer 2009).

## 7 Conclusion

In this paper, CM harmonics are re-parameterized by FEA and afterwards scaled by the phase current to artificially adopt the phenomena of saturation in the armature field within this practical approach. A demonstration on a PMSM shows, that this yields a flux density distribution which is in good agreement to FEA even in saturated and high saturated operation points.

## References

Binns, K. J. (1963). *Analysis and computaion of electric and magnetic field problems,*, Pergamon Press; [distributed in the Western Hemisphere by Macmillan, New York].

Hafner, M., Franck, D. & Hameyer, K. (2009). Quasistatic electromagnetic field computation by conformal mapping in permanent magnet synchronous machines, *17th Conference on the Computation of Electromagnetic Fields*, Florianopolis, Brazil.

Hanselman, D. C. (2003). *Brushless Permanent Magnet Motor Design*, 2 edn, The Writers' Collective.

Jacob, A. (1998). Zum einfluß von zahn- und jochsättigung auf die harmonischen des luftspaltfeldes, *Electrical Engineering (Archiv fur Elektrotechnik)* **81**(3): 151–161.

Rothe, R., van der Giet, M. & Hameyer, K. (2009). Convolution approach for analysis of magnetic forces in electrical machines, *8th International Symposium on Electric and Magnetic fields*, Mondovi, Italy, p. 91–92.

Seinsch, H. O. (1992). *Oberfelderscheinungen in Drehfeldmaschinen. Grundlagen zur analytischen und numerischen Berechnung*, Teubner Verlag.

van der Giet, M., Rothe, R. & Hameyer, K. (2009). Asymptotic fourier decomposition of tooth forces in terms of convolved air gap field harmonics for noise diagnosis of electrical machines, *COMPEL: The International Journal for Computation and Mathematics in Electrical and Electronic Engineering* **28**(4): 804–818.

Zarko, D., Ban, D. & Lipo, T. (2006). Analytical calculation of magnetic field distribution in the slotted air gap of a surface permanent-magnet motor using complex relative air-gap permeance, *Magnetics, IEEE Transactions on* **42**(7): 1828–1837.

Zarko, D., Ban, D. & Lipo, T. (2008). Analytical solution for cogging torque in surface Permanent-Magnet motors using conformal mapping, *Magnetics, IEEE Transactions on* **44**(1): 52–65.

Zhu, Z. & Howe, D. (1993). Instantaneous magnetic field distribution in brushless permanent magnet DC motors. III. effect of stator slotting, *Magnetics, IEEE Transactions on* **29**(1): 143–151.

Zhu, Z., Howe, D. & Chan, C. (2002). Improved analytical model for predicting the magnetic field distribution in brushless permanent-magnet machines, *Magnetics, IEEE Transactions on* **38**(1): 229–238.